Correlating the Efficiency and Nanomorphology of Polymer Blend Solar Cells Utilizing Resonant Soft X-ray Scattering

Hongping Yan,[†] Brian A. Collins,[†] Eliot Gann,[†] Cheng Wang,[‡] Harald Ade,[†,*] and Christopher R. McNeill[§,⊥,*]

[†]Department of Physics, North Carolina State University, Raleigh, North Carolina 27695-8202, United States, [‡]Advanced Light Source, Lawrence Berkeley National Laboratory, Berkeley, California 94720, United States, and [§]Cavendish Laboratory, University of Cambridge, JJ Thomson Avenue, Cambridge CB3 0HE, United Kingdom. [⊥]Present address: Department of Materials Engineering, Monash University, Clayton, Victoria 3800, Australia.

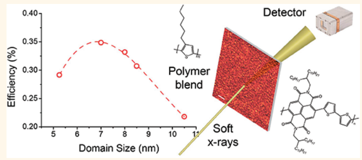

ABSTRACT Enhanced scattering contrast afforded by resonant soft X-ray scattering (R-SoXS) is used to probe the nanomorphology of all-polymer solar cells based on blends of the donor polymer poly(3-hexylthiophene) (P3HT) with either the acceptor polymer poly((9,9-dioctylfluorene)-2,7-diyl-*alt*-[4,7-bis(3-hexylthien-5-yl)-2,1,3-benzothiadiazole]-2′,2″-diyl) (F8TBT) or poly([*N*,*N*′-bis(2-octyldodecyl)-11-naphthalene-1,4,5,-8-bis(dicarboximide)-2,6-diyl]-*alt*-5,5′-(2,2′-12-bithiophene)) (P(NDI2OD-T2)). Both P3HT:F8TBT and P3HT:P(NDI2OD-T2) blends processed from chloroform with subsequent annealing exhibit complicated morphologies with a hierarchy of phase separation. A bimodal distribution of domain sizes is observed for P3HT:P(NDI2OD-T2) blends with small domains of size ∼5−10 nm that evolve with annealing and larger domains of size ∼100 nm that are insensitive to annealing. P3HT:F8TBT blends in contrast show a broader distribution of domain size but with the majority of this blend structured on the 10 nm length scale. For both P3HT:P(NDI2OD-T2) and P3HT:F8TBT blends, an evolution in device performance is observed that is correlated with a coarsening and purification of domains on the 5−10 nm length scale. Grazing-incidence wide-angle X-ray scattering (GI-WAXS) is also employed to probe material crystallinity, revealing P(NDI2OD-T2) crystallites 25−40 nm in thickness that are embedded in the larger domains observed by R-SoXS. A higher degree of P3HT crystallinity is also observed in blends with P(NDI2OD-T2) compared to F8TBT with the propensity of the polymers to crystallize in P3HT:P(NDI2OD-T2) blends hindering the structuring of morphology on the sub-10 nm length scale. This work also underscores the complementarity of R-SoXS and GI-WAXS, with R-SoXS measuring the size of compositionally distinguishable domains and GI-WAXS providing information regarding crystallinity and crystallite thickness.

KEYWORDS: bulk heterojunction · polymer blends · polymer solar cells · soft X-rays · X-ray scattering

Polymer solar cells are an interesting new approach to low-cost solar cells utilizing semiconducting polymers for the conversion of sunlight into electricity.[1] Since tightly bound excitons rather than free charges are the main product of photoexcitation, an important step in the energy conversion process is the dissociation of these excitons into electron−hole pairs at donor/acceptor interfaces. A number of donor/acceptor approaches are used, with fullerene derivatives,[1] inorganic nanocrystals,[2] along with electron-accepting polymers[3] used as electron acceptors in combination with an electron-donating polymer. The utility of a material as either an electron donor or acceptor depends on the material's electron affinity, with high electron affinity materials (in general) suited as electron acceptors and low electron affinity materials suited as electron donors. The designation is relative, however, with the same material being able to serve as an electron acceptor with one material and an electron donor with another depending on the relative electron affinities of the materials.[4] Limiting the effectiveness of these materials in exciton dissociation is the relatively short exciton diffusion length of ∼10 nm.[5] In order to absorb sufficient light (film thickness ∼100 nm or greater) while maintaining short distances to donor/acceptor interfaces, the bulk heterojunction concept has proved to be an effective approach. Here, thin film blends of donor and acceptor materials are produced that have sufficient intermixing between donor and acceptor to maintain charge generation (exciton dissociation) while (ideally) percolating interconnected pathways facilitate charge transport to the electrodes. The influence of morphology on device performance has been a topic of great interest to the organic photovoltaics community,[6−8] with film morphology affecting many device processes including charge generation,[9,10] interfacial charge separation,[11,12] and charge collection.[13] In general, a mixing of donor and acceptor on a length scale finer than the exciton diffusion length optimizes charge generation (exciton diffusion to and dissociation at donor/acceptor interfaces), while coarser morphologies optimize the separation of charges away from the interface and their collection at the device electrodes.

* Address correspondence to harald_ade@ncsu.edu, christopher.mcneill@monash.edu.

Received for review October 27, 2011 and accepted December 14, 2011.

Published online December 14, 2011
10.1021/nn204150f

© 2011 American Chemical Society

Polymer/fullerene solar cells have, to date, proved to be the most effective blend combination with power conversion efficiencies of over 8% now reported.[14] The efficiency of polymer/polymer solar cells in contrast has remained at ~2%,[4,15−18] largely attributed to inefficient interfacial charge separation[19−22] (that is, the recombination of electron−hole pairs localized at the donor/acceptor interface subsequent to charge transfer). However, the contribution of unoptimized morphology to this lackluster performance is not fully understood. In general, it is thought that a morphology consisting of interconnected pure phases with a characteristic domain size of ~10 nm (the exciton diffusion length) is most beneficial for device action.[13] A key challenge in the field of organic photovoltaics is the ability to provide quantitative information about the morphology of bulk heterojunction blends used in polymer solar cells. Even for polymer/fullerene solar cells whose morphology is easier to characterize due to differences in material density (and hence analysis by traditional techniques such as transmission electron microscopy), new discoveries are being made, such as the existence of a mixed phase in addition to pure polymer and pure fullerene phases in well-studied poly(3-hexylthiophene):[6,6]-phenyl-C_{61}-butyric acid methyl ester blends.[23−26] Transmission electron microscopy (TEM)[27−29] and atomic force microscopy (AFM)[30,31] have been the most common techniques for studying blend morphology; however, standard TEM has relatively poor chemical sensitivity and AFM is limited in being able to only provide information regarding surface topography that may or may not relate to bulk morphology. Energy-filtered TEM is increasingly being utilized that enhances the chemical sensitivity of TEM,[32−35] and neutron-based techniques are also being adopted to probe the structure of polymer/fullerene blends owing to the natural neutron scattering contrast between polymers and fullerenes.[26,36,37] X-ray scattering and diffraction using hard X-rays is also a useful technique providing information regarding molecular packing and the size of crystalline regions,[38,39] but scattering contrast from amorphous regions of different materials is low.

An alternative approach for enhanced chemical contrast with high resolution is the use of soft X-rays.[40,41] Photons with energy close to the 1s ionization energy of carbon are able to promote electrons from the 1s orbital of carbon to unoccupied electronic orbitals. Absorption resonances are observed that are associated with the unoccupied electronic structure of the polymer, providing a means for chemical contrast even when there is no difference in elemental composition. Scanning transmission X-ray microscopy (STXM)[42] that utilizes differences in the near-edge X-ray absorption spectra of materials for chemical contrast has been employed to provide two-dimensional composition maps of bulk heterojunction blends with sub-100 nm resolution.[43,44] The resolution of STXM is limited by the spot size achievable by zone-plate optics and by the inherent limitations associated with a two-dimensional projection of a 100 nm thick film. One way to overcome the limitations of zone-plate optics and two-dimensional imaging is to use material contrast afforded by soft X-rays in a scattering experiment. Recently, we have demonstrated the ability of resonant soft X-ray scattering (R-SoXS) to provide morphological information on the sub-10 nm length scale in conjugated polymer blends.[45] In this previous communication, blends of the polyfluorene derivatives poly(9,9′-dioctylfluorene-*co*-bis(*N*,*N*′-(4-butylphenyl))bis(*N*,*N*′-phenyl-1,4-phenylene)diamine) (PFB) and poly(9,9′-dioctylfluorene-*co*-benzothiadiazole) (F8BT) were studied that have been extensively studied with STXM. Our results revealed a hierarchy of phase separation in PFB:F8BT blends, with ~80 nm sized domains in as-cast samples that are readily observed by STXM, and a finer length scale of intermixing on the sub-10 nm length scale not readily observed by STXM but revealed by R-SoXS. With annealing, phase coarsening was initially observed on the length scale of a few to tens of nanometers followed by coarsening of the larger domains at higher temperatures.[45]

In this contribution, we utilize R-SoXS to study two more recently developed and more efficient polymer/polymer systems for which little detailed morphological information exists. In particular, we study blends of the donor polymer poly(3-hexylthiophene) (P3HT) with the acceptor polymer poly((9,9-dioctylfluorene)-2,7-diyl-*alt*-[4,7-bis(3-hexylthien-5-yl)-2,1,3-benzothiadiazole]-2′,2″-diyl) (F8TBT), along with blends of P3HT with the acceptor poly([*N*,*N*′-bis(2-octyldodecyl)-11-naphthalene-1,4,5,8-bis(dicarboximide)-2,6-diyl]-*alt*-5,5′-(2,2′-12-bithiophene)) (P(NDI2OD-T2)). P3HT:F8TBT blends represent one of the most efficient all-polymer solar cell systems to date,[4] while P3HT:P(NDI2OD-T2) blends[21] are of interest due to the exceptional electron mobility of P(NDI2OD-T2).[46] As a complement to the R-SoXS measurement, information about the crystal size and the qualitative degree of crystallization was derived from grazing-incidence wide-angle X-ray scattering (GI-WAXS) data. The combination of R-SoXS and GI-WAXS in particular serves as a powerful demonstration of the additional information derived from R-SoXS and the benefit of using separate techniques to probe amorphous and crystalline structure.

RESULTS AND DISCUSSION

Figure 1 presents the chemical structures of P3HT, F8TBT, and P(NDI2OD-T2) and the optical absorption spectra of neat films. P3HT and F8TBT have overlapping absorption bands in the visible region peaking at ~550 nm, while P(NDI2OD-T2) has a low-energy charge-transfer absorption band peaking at 700 nm and extending into the near-infrared. The absorption spectrum of amorphous F8TBT is featureless, while

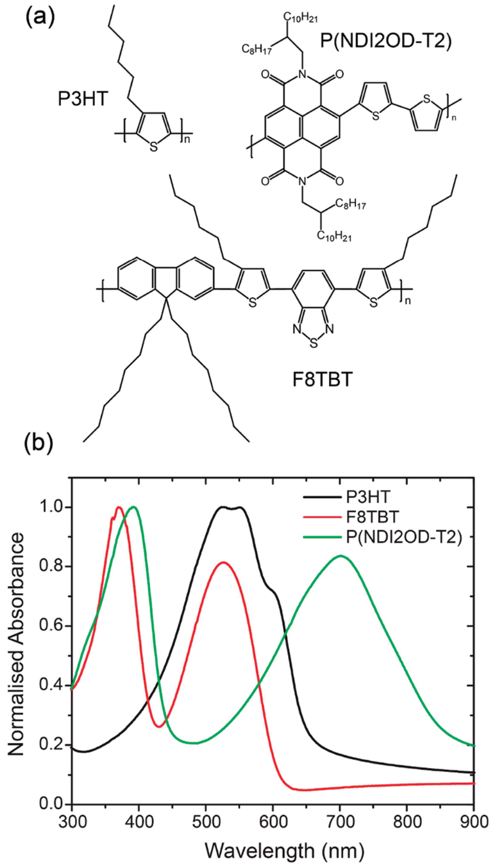

Figure 1. (a) Chemical structures of P3HT, F8TBT, and P(NDI2OD-T2). (b) Absorption spectra of neat films.

the absorption spectra of semicrystalline P3HT and P(NDI2OD-T2) show features associated with vibronic structure that may be related to film microstructure.[47,48] Figure 2 presents the evolution of the absorption spectra of 1:1 (by weight) blend films of P3HT:F8TBT and P3HT:P(NDI2OD-T2) with annealing. These films were prepared in the same fashion using the same annealing protocol as for films used in devices and films used for structuring characterization, with all blends processed from chloroform. All films were annealed for 10 min followed by quenching to room temperature and subsequent measurements. For P3HT:F8TBT films, there is little vibronic structure in the P3HT absorption component in as-cast films, but with annealing, P3HT vibronic structure appears consistent with ordering of the P3HT phase.[49,50] The vibronic structure in the UV−vis spectra of the annealed P3HT:F8TBT films is less prominent than that observed in neat P3HT reference shown in Figure 1. While overlap of the P3HT and F8TBT absorption spectra will make the P3HT vibronic structure less noticeable in blend spectra, the vibronic structure present in these chloroform-processed films is less prominent than observed in xylene-processed blends,[50] suggesting that P3HT crystallization is hindered (see Figure S1 in the Supporting Information). For P3HT:P(NDI2OD-T2) films, a similar evolution in P3HT vibronic structure with annealing is observed, accompanied by changes in the structure of the P(NDI2OD-T2) absorption component. The vibronic structure of the P3HT phase is similar to that observed in neat P3HT, suggesting that P3HT crystallization is not hindered here. Curiously, annealing the P3HT:P(NDI2OD-T2) film at 200 °C results in a loss of structure in the absorption spectrum of both components, suggesting a melting of polymer chains and some loss of crystallinity, which has been confirmed by a comparison of GI-WAXS data of 180 and 200 °C annealed samples (see Figure S2 in Supporting Information). A loss of P3HT crystallinity due to melting with annealing at 200 °C in P3HT:[6,6]-phenyl-C_{61}-butyric acid methyl ester (PCBM) blends has also been observed by Verploegen *et al.*[51]

Figure 3 presents the evolution of the device characteristics of P3HT:F8TBT and P3HT:P(NDI2OD-T2) photovoltaic devices with annealing. All devices were fabricated with PEDOT:PSS-coated ITO glass substrates and aluminum top electrodes (see the Experimental Section for full details). Both P3HT:F8TBT and P3HT:P(DNI2OD-T2) devices show a pronounced evolution of device performance with annealing. P3HT:F8TBT devices show a dramatic 50-fold increase in power conversion efficiency from 0.018% for unannealed devices to 0.90% for devices annealed at 180 °C. This increase is brought about by changes in both short-circuit current (a 20-fold increase) and fill factor (increase from 0.22 to 0.4). P3HT:P(NDI2OD-T2) devices show an increase in power conversion efficiency from 0.16% for unannealed devices to 0.35% for devices annealed at 140 °C. Although the short-circuit current (J_{sc}) of P3HT:P(NDI2OD-T2) devices peaks at an annealing temperature of 160 °C, corresponding to a 3-fold increase, device performance is undermined by a monotonic decrease in the fill factor (FF) with annealing decreasing from 0.48 for unannealed films to 0.22 for films annealed at 200 °C. Device efficiencies are consistent with previous reports,[4,21] though we note that optimized P3HT:F8TBT devices typically have a slightly thinner active layer (70 nm compared to 100 nm here) and are prepared from xylene rather than chloroform. Chloroform is used here as it results in a more intimate initial mixing of the blend components, producing a more dramatic change in device efficiency and hence facilitating study of the influence of the evolving nanomorphology during annealing on device performance. The lower P3HT crystallinity in chloroform-processed devices may also partially explain the lower efficiency of these devices, with the interplay between nanomorphology and crystallinity discussed further below. Interestingly, the current-voltage (*J*−*V*) curves of the P3HT:F8TBT and P3HT:P(NDI2OD-T2) devices show a very different shape evolution. Although the J_{sc} of both P3HT:F8TBT and P3HT:P(NDI2OD-T2) devices is maximized for an anneal temperature of ∼160−180 °C, the FF of the P3HT:F8TBT devices increases monotonically

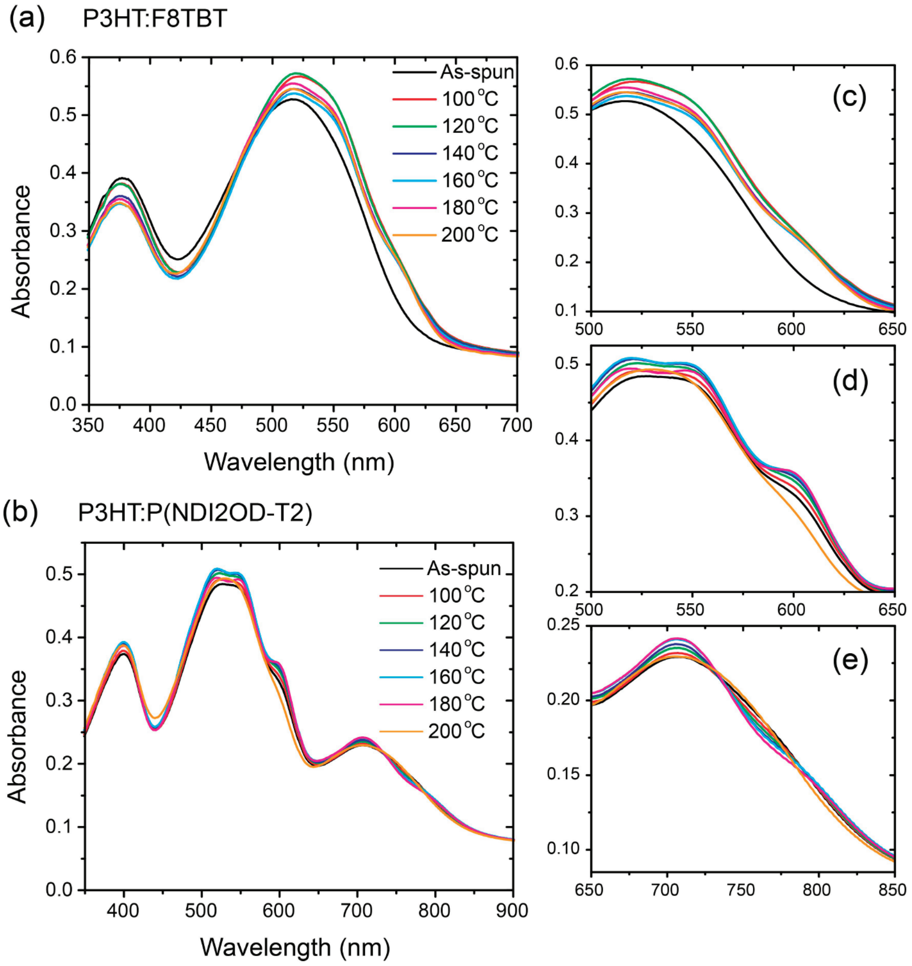

Figure 2. Evolution of the absorption spectra of blend films with annealing: (a) P3HT:F8TBT; (b) P3HT:P(NDI2OD-T2). (c) Changes in P3HT vibronic structure with annealing in the P3HT:F8TBT blend; (d,e) changes in P3HT and P(NDI2OD-T2) vibronic structure in the P3HT:P(NDI2OD-T2) blend with annealing.

with annealing while it decreases monotonically with annealing for the P3HT:P(NDI2OD-T2) devices. One reason behind the dramatic improvement in P3HT:F8TBT device efficiency with annealing (both in terms of J_{sc} and FF) is the improvement in P3HT ordering that increases hole mobility.[50,52] Annealing of P3HT:F8TBT blends spin-coated from xylene leads to an increase in hole mobility of an order of magnitude.[52] A more dramatic enhancement of mobility is expected for P3HT:F8TBT blends processed from chloroform as the P3HT fraction is more disordered in as-cast films from chloroform. This increase in mobility leads to enhanced charge separation efficiency resulting in both increased J_{sc} and FF. For P3HT:P(NDI2OD-T2) blends, a significant portion of the P3HT component is already ordered (see also GI-WAXS results below), meaning that there is less likely to be as dramatic an improvement in hole mobility with annealing.

Figure 4 shows the R-SoXS scattering profiles of P3HT:P(NDI2OD-T2) blend thin films prepared under various conditions, that is, as-spun and annealed at 100, 120, 160, 180, and 200 °C. The data were acquired at 285.3 eV, an energy for which the chemical contrast between the two polymers is optimized in relation to mass–thickness differences (see Supporting Information). Scanning transmission X-ray microscopy (STXM) data showed that the average composition of the ~180 nm spaced domains does not evolve with annealing (see Figure S5 in the Supporting Information). The R-SoXS data have thus been normalized to the scattering intensity of the low q peak at ~0.04 nm^{-1}. To avoid confusion, some low q data (<0.02 nm^{-1}) that are distorted by parasitic scattering from a few dispersed, large agglomerates or impurities in the 100 and 160 °C samples are removed in the figure. Such sample imperfections are readily observed and correlated with visible light microscopy. The near complete constancy of the shape and position of the low q peak is a further indication that domains corresponding to this domain size do not evolve in size or average composition. Overall, with the exception of the as-spun film, a bimodal size distribution is observed for all films, with domains corresponding to ~5–10 and ~75–100 nm, respectively. For the as-spun film, only domains ~75–100 nm in size are observed. (We note that the top scale in Figure 4 is the domain spacing. Hence, for a morphology with near equal volume fractions, the

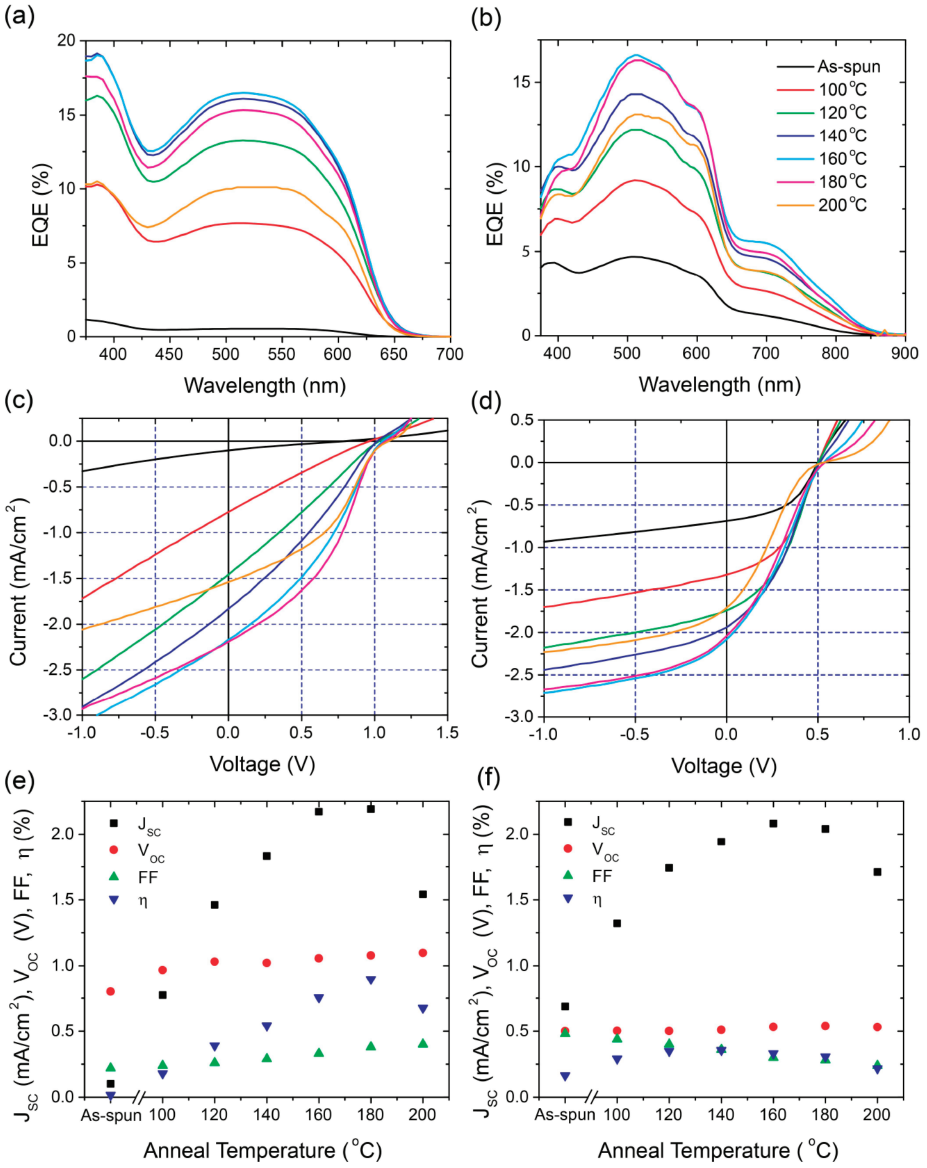

Figure 3. Evolution of the device characteristics of ITO/PEDOT:PSS/P3HT:F8TBT/Al (a,c,e) and ITO/PEDOT:PSS/P3HT:P(NDI2OD-T2)/Al (b,d,f) devices with annealing. (a,b) Changes in the external quantum efficiency spectra, (c,d) plot of the current voltage characteristics under 100 mW/cm^2 AM1.5G illumination, and (e,f) summary of the evolution in short-circuit current, open-circuit voltage, fill factor, and power conversion efficiency with annealing temperature.

domain size is a factor of 2 smaller.) Scattering can, by its very nature, not create a reconstruction of the real-space structure. It is thus incapable of differentiating easily (a) if small domains are subdomains of large domains or (b) if different regions in space have large domains and others have small domains. Given the complexity of these system and the limited information, we will discuss the morphology in terms of ensemble averages only and will refrain from explicit interpretation in terms of specific hierarchical structures as have been recently proposed in fullerene based devices.[53] In contrast to the larger domains, the smaller domains show a clear change in size with annealing, with the domain size systematically increasing with annealing temperature (see inset to Figure 4). Interestingly, the size of these small domains is generally on the order of the exciton diffusion length, evolving from ∼5 nm for the 100 °C annealed film to ∼10 nm for the 200 °C annealed film. Device efficiency is optimized for anneal temperatures of 160−180 °C corresponding to a domain spacing of ∼8−9 nm. In addition to information regarding the domain spacing provided by the position of the scattering peaks, the scattering intensity also provides qualitative information regarding the purity and volume fraction of the domains. The maximum scattering intensity for the small domains is observed for samples annealed at 160 °C, which corresponds to the maximum observed in J_{sc}. While the scattering data provide information regarding domain spacing and purity, it does not provide information regarding the connectivity of domains. For the 200 °C annealed film, the domain spacing only

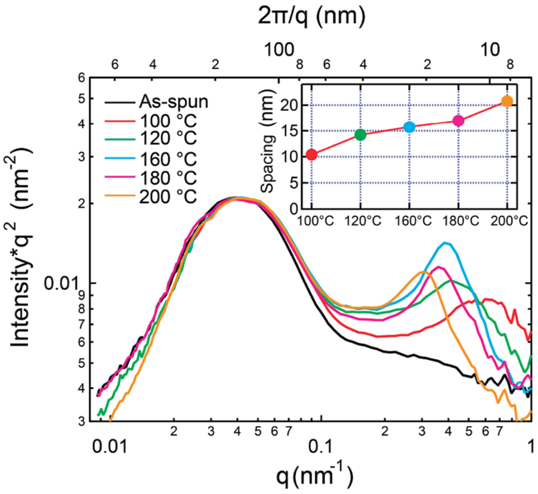

Figure 4. R-SoXS of P3HT:P(NDI2OD-T2) blend thin films prepared at various conditions: as-cast, 120, 160, 180, and 200 °C annealed. Inset: Domain spacing calculated from the fitted scattering peak locations of the smaller domains.

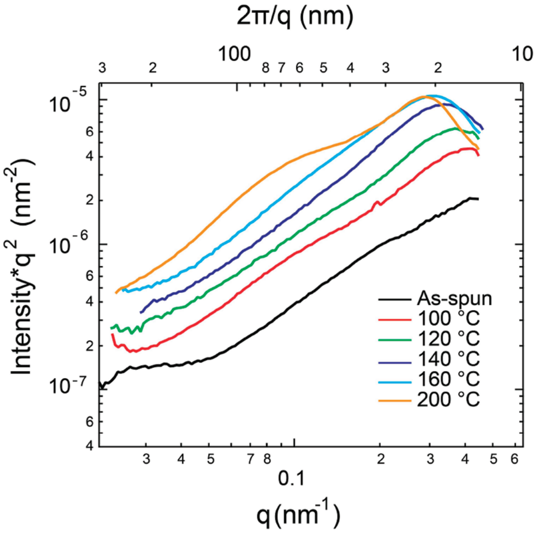

Figure 5. R-SoXS of P3HT:F8TBT blend thin films prepared at various conditions: as-cast and annealed at 100, 120, 140, 160, and 200 °C.

increases to ∼10−11 nm with a mild reduction in scattering intensity, yet 200 °C annealed devices exhibit a pronounced drop in efficiency and the appearance of an "S-shape" in the *J*−*V* curve about open circuit. The reduced performance of the 200 °C annealed device could result from domains with poor connectivity, consistent with the production of S-shaped *J*−*V* curves *via* the accumulation of space charge at material interfaces.[54] Alternatively, the reduced crystallinity in the 200 °C annealed device (see Figure S2 in the Supporting Information) is likely to result in lower charge carrier mobilities and reduced charge separation and collection.

The P3HT:F8TBT blend has a rather different morphology. Figure 5 shows the R-SoXS data acquired on this system at 285.5 eV for as-spun, 100, 120, 160, 180, and 200 °C annealed samples. Analogous to P3HT:P(NDI2OD-T2) blends, 285.5 eV is the energy where the polymer/polymer contrast is optimized for P3HT:F8TBT (see Supporting Information). Here, we observe a broader domain size distribution than for P3HT:P(NDI2OD-T2). A peak corresponding to ∼7 nm domains is evident with annealing at 100 °C, with a gradual increase in average domain size to 11 nm for annealing at 200 °C. At the same time, the intensities increase for all but the highest *q* values due to uniform coarsening and purification of all the structures. Only at the highest annealing temperature of 200 °C does a clear secondary feature corresponding to ∼30 nm domains emerge. Furthermore, the smaller domains are significantly more numerous or more pure in relation to large domains as indicated by the high scattering intensity at high *q*. Whereas in the P3HT:P(NDI2OD-T2) blend, the high *q* peak near $q = 0.4\ \text{nm}^{-1}$ has a scattering intensity of only about 50% that of the low *q* peak at $0.04\ \text{nm}^{-1}$, the scattering intensity from domains of ∼10 nm in size in P3HT:F8TBT is more than an order of magnitude higher than those 50 nm or larger. Peak efficiency and peak J_{sc} are observed at 180 °C, which corresponds (by inference, as this particular temperature is missing in the data set in this sample series, although is confirmed from data of samples with slightly larger thickness) to a saturation of intensity of the ∼10 nm domains, limited domain growth, and onset of the development of ∼30 nm domains. Overall, the average domains in the P3HT:F8TBT blend are significantly smaller than in the P3HT:P(NDI2OD-T2) blend and nearly matched to the exciton diffusion length.

Figure 6 presents the photoluminescence (PL) spectra of P3HT:F8TBT films as a function of annealing. Due to the characteristic length scale associated with exciton diffusion (∼10 nm), PL data provide qualitative information regarding domain size on the 10 nm length scale. Due to the low PL quantum efficiency (PLQE) of P(NDI2OD-T2), a similar analysis could not easily be performed on P3HT:P(NDI2OD-T2) films. Neat F8TBT has a PLQE of 27% and is more luminescent than that of neat regioregular P3HT that is measured to have a PLQE of 1.8%. Examining the data of Figure 6, as-spun films have a PLQE of 3.8%, indicating efficient quenching of F8TBT emission *via* exciton dissociation at P3HT/F8TBT heterojunctions. With annealing to 100 °C a sharp drop in PLQE to 2.1% is observed that can be attributed to aggregation of P3HT.[50] The photophysics of P3HT is highly sensitive to polymer conformation with disordered, regiorandom P3HT possessing a significantly higher PLQE (∼15%) to ordered, regioregular P3HT.[50] Subsequent annealing leads to a monotonic increase in PLQE with annealing consistent with the evolution of morphology on a 10 nm length scale. Even at an annealing temperature of 200 °C, the PLQE of the blend is still well below that of neat F8TBT, suggesting that there is still significant intermixing on the 10 nm length scale. For comparison, PFB:F8BT blends annealed at 200 °C have a PLQE similar to the PLQE neat

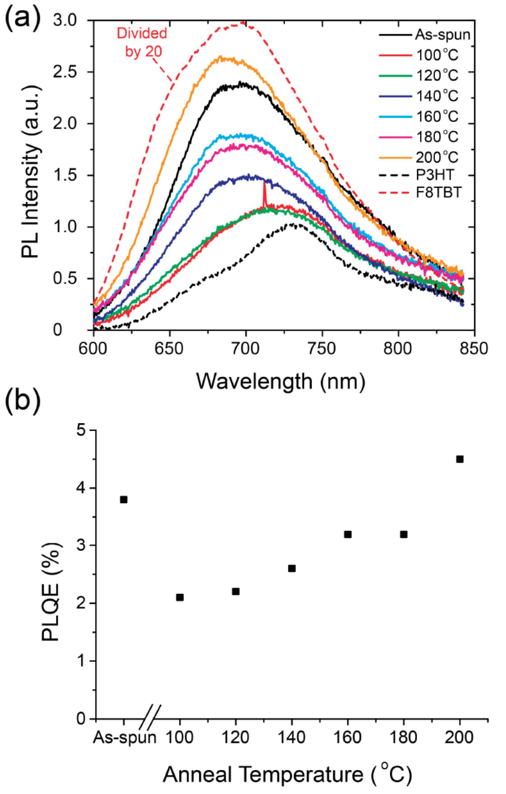

Figure 6. Evolution of the photoluminescence spectrum of P3HT:F8TBT blends with annealing. Solid lines depict the blend; while dashed lines correspond to the spectrum of neat films. The magnitude of the F8TBT spectrum has been reduced 20-fold.

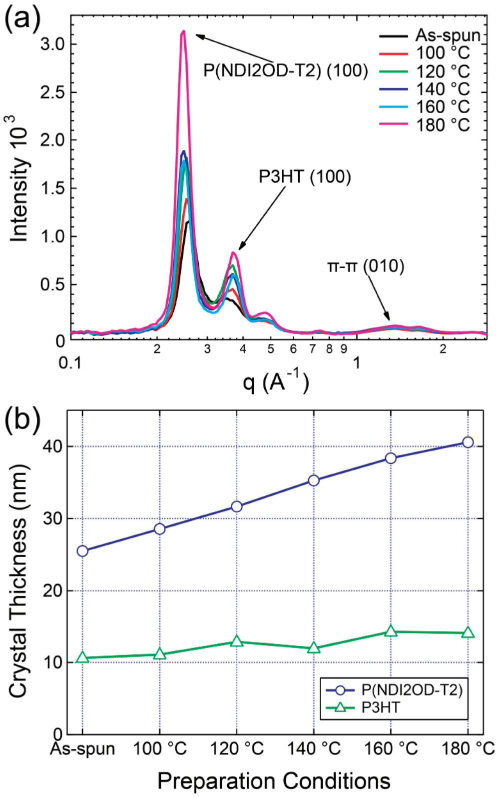

Figure 7. In-plane GI-WAXS data of P3HT:P(NDI2OD-T2) samples prepared at various conditions: as-spun, 100, 120, 140, 160, and 180 °C annealed (a), and crystal sizes along the (100) direction derived from a Scherrer analysis (b).

F8BT (66%), indicating the evolution of pure domains with spacing much larger than the exciton diffusion length, confirmed by STXM and R-SoXS measurements.[9,43] The PL data of Figure 6 are consistent with the R-SoXS data where an evolution in nanostructure on the length scale of 5−10 nm is directly observed but with limited structural evolution beyond the exciton diffusion length. Note that PL measurements are limited in what they can say regarding morphology, as they are sensitive to small minority concentrations and provide no information on length scales much larger than the exciton diffusion length. Thus PL measurements cannot distinguish between large domains with a small minority component that still efficiently quenches PL and efficient PL quenching by pure domains but with domain spacing less than the exciton diffusion length.

To derive information about crystallinity and crystallite thickness in the thin film blends, GI-WAXS data were acquired. Figure 7a shows the in-plane scattering intensity of P3HT:P(NDI2OD-T2) as-spun samples and those annealed at 100, 120, 140, 160, and 180 °C. Utilizing reference measurements on pure films, the peaks near $q = 0.25, 0.37$, and 1.7 Å^{-1} are indexed as the P(NDI2OD-T2) (100), the P3HT (100), and the P3HT $\pi-\pi$ (010) peaks, respectively. The relative intensity changes of the P(NDI2OD-T2) (100) peak and the P3HT (100) peak indicate that P(NDI2OD-T2) crystallizes first or more readily in the as-spun films. The out-of-plane scattering shows a similar evolution, but we include here the in-plane GI-WAXS results to allow a comparison to the R-SoXS data which only measures the in-plane morphology. By performing a Scherrer analysis on (100) peaks and correcting the instrumental broadening, the size of the crystals along those crystallographic directions were derived and plotted in Figure 7b. Crystal size is observed to evolve with annealing temperature, qualitatively mirroring the R-SoXS observations. However, the size of the P(NDI2OD-T2) crystals even in as-spun films is much larger than the small domains observed in R-SoXS. These crystallites therefore must be embedded in the larger 75−100 nm domains observed by R-SoXS. Similarly, the size of the P3HT crystallites, especially in as-spun and mildly annealed films, are larger than the smaller domains observed by R-SoXS. These observations underscore the fact that R-SoXS measures a different aspect of materials than GI-WAXS and that these two characterization methods are complementary. GI-WAXS only measures the crystal size along the (100) direction, providing little information about the size along the other directions or direct information about whether the crystals are embedded in the same or the complementary material. In contrast, R-SoXS measures the size of the compositionally distinguishable domains, which does not correspond

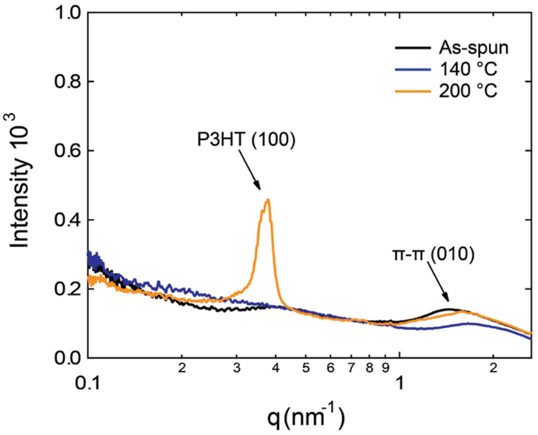

Figure 8. In-plane GI-WAXS data of P3HT:F8TBT samples prepared at various conditions: as-spun, 140, and 200 °C annealed.

to the size measured with GI-WAXS of either the P3HT or the P(NDI2OD-T2) crystals. Furthermore, GI-WAXS detects crystallization in as-cast films, whereas R-SoXS does not detect structure at the related length scale. The discrepancy observed indicates that most of the crystals are surrounded by the same polymer within the large domains observed in R-SoXS. Consequently, only a fraction of the volume of the P3HT:P(NDI2OD-T2) devices has a favorable domain size that is on the order of the exciton diffusion length. It is also highly likely that the small domains observed with R-SoXS are predominantly composed of amorphous P3HT and P(NDI2OD-T2), although definitive analysis on the relative volume fraction of crystalline and amorphous domains of each polymers cannot be provided at this point. In addition, a direct comparison of the GI-WAXS data from 180 and 200 °C annealed films shows that the latter has much less crystallinity, which explains the loss of structure in the optical absorption spectrum mentioned at the beginning of the Results and Discussion section.

In contrast to the P3HT:P(NDI2OD-T2) blends, significantly less crystallization was revealed in P3HT:F8TBT blends with GI-WAXS, as shown in Figure 8, in which data from as-spun, 140, and 200 °C P3HT:F8TBT thin films are plotted. Only a broad and small P3HT (100) diffraction peak at $q \approx 0.37$ Å^{-1} is observed for the 200 °C annealed film. Furthermore, the P3HT crystals are so small or ill-formed that the (010) (*i.e.*, $\pi-\pi$ stacking) peak is barely detectable. The appearance of vibronic structure in the absorption spectrum of the 140 °C annealed film (Figure 2) may be attributed to molecular aggregation of P3HT without the formation of coherent crystallites. In Figure 8, there is no diffraction peak that can be attributed to F8TBT.

Annealing at various temperatures causes different structural changes in the two blends. The morphological evolution and the crystallization behavior can be summarized and correlated to device performance as follows. P3HT:F8TBT blends do not exhibit any dominant large-scale phase separation and little crystallization for all annealing temperatures. The vast majority of this material is structured at the ~10 nm length scale. The best device performance is correlated to the arrest in growth and purification of the ~10 nm domains and just prior to the emergence of domains with a second length scale of about 30 nm, possibly being the result of coalescence. This optimum morphology is consistent with the results of device simulations that indicate that a morphology with domain size slightly larger than the exciton diffusion length balances the processes of charge generation and charge separation.[11] In contrast, P3HT:P(NDI2OD-T2) blends have a more unfavorable morphology if viewed from the conventional bulk heterojunction structure model with dominant domain size of ~90 nm even in the as-cast blends. These domains are much larger than the exciton diffusion length resulting in the loss of photoexcitations *via* exciton recombination. The high crystallinity in the P3HT:P(NDI2OD-T2) blends impedes large-scale evolution of the morphology during annealing. Within the annealing sequence investigated, high scattering intensity for ~9 nm domains corresponded to the highest J_{sc}. Although domains in size on the order of the exciton diffusion length develop, only a fraction of the material is structured at that length scale.

The P3HT:F8TBT blend can and does evolve more than the P3HT:P(NDI2OD-T2) blend since this system is less crystalline at all preparation conditions than the P3HT:P(NDI2OD-T2) blends. The suppression of the crystallization of the P3HT in P3HT:F8TBT blends relative to P3HT:P(NDI2OD-T2) blends implies that there might be a favorable interaction at the molecular level between P3HT and F8TBT that results in partial miscibility of this system. Indeed, a previous X-ray diffraction study of thick P3HT:F8TBT films has found evidence for F8TBT intercalation in P3HT crystallites.[49]

If better control of the morphology can be accomplished for P3HT:P(NDI2OD-T2), significant improvement might be achieved for that system. The high crystallinity might allow the morphology to be frozen in, thus making the annealing step relatively insensitive to details of the fabrication protocol. Such increased processing latitude might be important for large scaling fabrication processes such as roll-to-roll printing. Crystallite size, however, has to be commensurate with the dimensions required for efficient device operation. The 25–40 nm size of the P(NDI2OD-T2) crystals in the P3HT:P(NDI2OD-T2) blends precludes their incorporation in the finer nanostructure that is arguably more important for device operation. Indeed, the potential lack of crystallinity within the 5–10 nm domains in P3HT:P(NDI2OD-T2) may help to explain the poor performance of P3HT:P(NDI2OD-T2) solar cells that has partly been attributed to fast interfacial recombination following charge transfer.[21]

Assuming that a significant proportion of the interfacial area is attributable to the smaller 5–10 nm domains, a lack of molecular order in these domains is likely to be detrimental to charge separation. Ordered crystallites should favor charge separation due to increased molecular order and the associated charge mobility. Thus, while neat P(NDI2OD-T2) possesses an electron mobility comparable to that of PCBM, this high electron mobility may not be imparted locally to disordered P(NDI2OD-T2) chains at donor/acceptor interfaces within the smaller domains. These observations highlight that while material crystallinity in general is thought to be favorable, enabling high carrier mobilities, it can be problematic by disabling formation of morphology on the desired length scale.

It is interesting to note that the near-optimal morphology of the P3HT:F8TBT blend does not lead, however, to a much superior J_{sc} when compared to the P3HT:P(NDI2OD-T2) blend. The J–V curves of optimized P3HT:F8TBT devices still have a steep gradient even out to −1 V reverse bias (Figure 3c), indicating that while near-optimum morphologies have been achieved interfacial charge separation is still limiting device performance. The J–V curves of P3HT:P(NDI2OD-T2) devices are not as steep in contrast, suggesting that charge separation is not as problematic for P3HT:P(NDI2OD-T2) and that the large domains may also be limiting device performance through incomplete exciton dissociation. Indeed, relatively high fill factors have been achieved for P3HT:P(NDI2OD-T2) blends (up to 67%);[55] however, these fill factors have not been combined with high short-circuit currents. The lower overall performance of the P3HT:P(NDI2OD-T2) system compared to P3HT:F8TBT can be primarily traced to a lower open-circuit voltage and to a lesser extent to reduced fill factor for conditions that produced the higher short-circuit currents. Ultimately, it is the electronic structure and the resultant low open-circuit voltage of the P3HT:P(NDI2OD-T2) blend that is the major difference. While the P(NDI2OD-T2) infrared band extends the absorption of the P3HT:P(NDI2OD-T2) blend relative to the P3HT:F8TBT system, it has insufficient absorption strength in ~100 nm thick films to provide a decisive advantage.

CONCLUSIONS

Resonant soft X-ray scattering has been employed to directly correlate the device performance of polymer solar cells with the evolution of nanostructure on the length scale of 5–20 nm. For the two all-polymer solar cell systems investigated, significant differences in the nature and evolution of nanostructure were observed. For P3HT:P(NDI2OD-T2) blends, a bimodal domain structure was observed with characteristic domain sizes of ~75–100 and ~5–10 nm. The size of the larger domains in the P3HT:P(NDI2OD-T2) blends was observed to be invariant under annealing, while the smaller domains were observed to evolve from ~5 nm for 100 °C annealed films to ~10–11 nm for 200 °C annealed films. For P3HT:F8TBT blends, no dominant large-scale phase separation was observed with the vast majority of the material structured at the ~10 nm length scale. A broader domain size distribution on the 10 nm length scale was observed for P3HT:F8TBT compared to P3HT:P(NDI2OD-T2), with annealing leading to a gradual increase in the average domain size from ~7 nm (100 °C) to ~11 nm (200 °C). Only with annealing at 200 °C was a secondary feature corresponding to a ~30 nm domain size observed. For both systems, the optimization of device performance with annealing was correlated with a coarsening and purification of domains on the 5–10 nm length scale, consistent with the creation of a morphology that balances charge separation/collection with exciton dissociation.

GI-WAXS was used to provide complementary information regarding crystallinity and crystallite size, revealing a higher crystallinity of P3HT in blends with P(NDI2OD-T2) than in blends with F8TBT. Embedded in the larger 75–100 nm domains, 25–40 nm P(NDI2OD-T2) crystallites were observed–significantly larger than the optimum domain size for exciton dissociation. Thus the propensity of P3HT and P(NDI2OD-T2) to crystallize in P3HT:P(NDI2OD-T2) blends hampers the formation of nanostructure on the desired length scale resulting in a suboptimal morphology. The lower crystallinity of P3HT in blends with F8TBT suggests a favorable interaction between P3HT and F8TBT at the molecular level enabling formation of a near-optimum morphology. These observations demonstrate that, while crystallinity is thought to be desirable in enabling high carrier mobilities and arresting large-scale phase separation, control over crystallite size is required to enable formation of domains on the length scale of the exciton diffusion length. The formation of large domains in P3HT:P(NDI2OD-T2) blends driven by crystallization hampers the performance of this system with improved control of nanostructure a route to improved efficiency. Our study also highlights the utility of R-SoXS in providing complementary information to GI-WAXS enable a more complete picture of nanomorphology to be captured.

EXPERIMENTAL SECTION

Materials. P3HT was supplied by Merck KGaA with molecular weight (M_w) of 25 kg/mol, polydispersity index (PDI) of 2.0, and regioregularity of 94%. P(NDI2OD-T2) was purchased from Polyera Corp. (ActivInk N2200) with a specified number-average molecular weight (M_n) of 25.4 kg/mol and PDI of 4.0. F8TBT was supplied by Cambridge Display Technology Ltd. with a peak molecular weight (M_p) of 432 kg/mol. Blend films for devices, optical characterization, and X-ray scattering were prepared in identical fashion. P3HT:F8TBT blends were prepared from anhydrous chloroform with a weight ratio of 1:1 and total solution concentration of 12 g/L. Spin-coating at 4000 rpm yielded P3HT:F8TBT films with a thickness of 100 ± 20 nm. P3HT:P(NDI2OD-T2) blends were also prepared from anhydrous chloroform with a 1:1 weight ratio but with a total solution concentration of 19 g/L to produce films 105 ± 5 nm thick when spin-coated at 4000 rpm. Film thicknesses were determined using a Dektak 6 M profilometer.

Optical Characterization. Films for optical absorption and photoluminescence analysis were prepared on quartz substrates. Absorption spectra were acquired using a Hewlett-Packard 8453 diode-array spectrometer. PL spectra and efficiencies were measured at room temperature in a nitrogen-purged integrating sphere with excitation from an argon ion laser at 488 nm and detection with an Oriel Instaspec IV spectrometer.

Device Fabrication. Devices were prepared by spin-coating blend films on PEDOT:PSS-coated indium−tin−oxide glass substrates. The ITO-covered glass substrates were initially cleaned by solvent cleaning and oxygen plasma treatment. PEDOT:PSS (40 nm thick) was then deposited by spin-coating onto the plasma-treated substrates and then annealing at 120 °C before being transferred to a nitrogen glovebox for spin-coating of P3HT:F8TBT and P3HT:P(NDI2OD-T2) layers. Previous X-ray photoelectron experiments have shown that P3HT preferentially wets the PEDOT/PSS surface for both P3HT:F8TBT and P3HT:P(NDI2OD-T2).[21,50] After the active blend layer was deposited, the samples were transferred to a vacuum evaporator inside the glovebox where 100 nm thick aluminum electrodes were evaporated through a shadow mask. Annealing was performed on a hot plate within the glovebox prior to encapsulation.

Device Characterization. External quantum efficiency was measured as a function of wavelength by dispersing light from a tungsten filament (Newport 250 W QTH) through a monochromator (Oriel Cornerstone 130) with a spot size smaller than the device active area. Light intensities of less than 1 mW cm^{-2} were used with the short-circuit current recorded using a Keithley 2635 source measure unit. Current−voltage characteristics were measured under an equivalent of 100 mW cm^{-2} AM1.5G illumination with an ABET class AAA solar simulator correcting for spectral mismatch.

Resonant Soft X-ray Scattering Measurements. Scattering measurements were performed at beamline 11.0.1.2 at the Advanced Light Source.[56] This undulator beamline is equipped with a variable line spacing plane grating monochromator and a four-bounce harmonic rejection assembly composed of four SiO_2 substrates coated with 30 nm nickel for the sake of spectral purity. To eliminate most of the beamline parasitic scatter, a set of four-jaw collimating slits were used to define the beam. The scattered intensity was recorded by a back illuminated Princeton PI-MTE CCD thermoelectrically cooled to −45 °C. Beam centering was completed by imaging the direct beam on the CCD while attenuated with a carbon film. Sample−detector distance was measured from diffraction peaks of the triblock copolymer poly(isoprene-*b*-styrene-*b*-2-vinyl pyridine), which has a known spacing of 391 Å at 280 eV. The beam size at the sample is approximately 300 μm by 200 μm. A modified version of the NIKA software package was used to process the scattering data to (i) subtract background, (ii) normalize by the I_0 provided by photodiode, and (iii) make solid angle corrections. The acquisition time was 60 s for low q region (below 0.5 nm^{-1}) and 120 s for high q region (above 0.5 nm^{-1}). These two regions were then stitched together with detector dwell time correction applied.

Removal of parasitic scattering was aided by investigating known isotropic scattering samples and comparing the scattering signals derived by integrated over 8° sectors and eliminating any regions and sectors containing data disagreeing with the others. The parasitic scattering is caused by a few dispersed, large agglomerates or impurities. They are readily observed with visible light microscopy. The scattering intensity profiles were scaled by q^2 to represent total scattered intensity at a given q.

The sample films used for R-SoXS were spin-cast on NaPSS-covered glass as substrate. To carry out R-SoXS experiment in transmission, the film is floated off in deionized water and picked up with a 1.5 mm by 1.5 mm silicon nitride window. The film is then dried in air before being transferred into the vacuum chamber for R-SoXS.

Grazing-Incidence Wide-Angle X-ray Scattering (GI-WAXS). GI-WAXS experiment was performed at beamline 7.3.3 of Advanced Light Source.[57] The blend films were prepared on PEDOT:PSS-covered glass substrates, following the same protocol used preparing samples for other characterizations. Although the data were acquired on samples with slightly larger thickness, ∼140 nm, instead of ∼100 nm used for other characterizations, we have confirmed that there is no observable GI-WAXS data difference between samples due to this small thickness difference other than overall intensity. The 10 keV X-ray beam was incident at a grazing angle of 0.12°, which maximized the scattering intensity from the samples. The scattered intensity was detected with an ASDC Quantum 4 CCD.

Scanning Transmission X-ray Microscopy. STXM measurements were performed at beamline 5.3.2 of the Advanced Light Source (ALS), Berkeley, CA.[58] The silicon frame-supported films were mounted in the sample chamber which was evacuated to 0.3 mbar and subsequently refilled with 1/3 atm of helium. The intensity of the focused X-ray beam transmitted through the film was recorded using a scintillator and photomultiplier tube and measured as a function of energy and position.

Acknowledgment. This work was supported in the UK by the EPSRC (EP/E051804/1) and in Australia by the ARC (FT100100275). NCSU's contribution (GI-WAXS, R-SOXS) is supported by DOE, OS, BES, MSE (DE-FG02-98ER45737). Data were acquired at beamlines 11.0.1.2, 7.3.3, and 5.3.2.2 at the ALS, which is supported by DOE (DE-AC02-05CH1123). The authors thank Cambridge Display Technology Ltd. for the supply of F8TBT.

Supporting Information Available: Absorption spectra of as-cast chloroform and xylene P3HT:F8TBT blends; comparison of GI-WAXS data of 180 and 200 °C annealed P3HT:P(NDI2OD-T2) blends; details of optimization of R-SoXS energy; STXM analysis of domain size. This material is available free of charge *via* the Internet at http://pubs.acs.org.

REFERENCES AND NOTES

1. Brabec, C. J.; Gowrisanker, S.; Halls, J. J. M.; Laird, D.; Jia, S.; Williams, S. P. Polymer−Fullerene Bulk-Heterojunction Solar Cells. *Adv. Mater.* **2010**, *22*, 3839–3856.
2. Dayal, S.; Kopidakis, N.; Olson, D. C.; Ginley, D. S.; Rumbles, G. Photovoltaic Devices with a Low Band Gap Polymer and CdSe Nanostructures Exceeding 3% Efficiency. *Nano Lett.* **2010**, *10*, 239–242.
3. McNeill, C. R.; Greenham, N. C. Conjugated-Polymer Blends for Optoelectronics. *Adv. Mater.* **2009**, *21*, 3840–3850.
4. McNeill, C. R.; Abrusci, A.; Zaumseil, J.; Wilson, R.; McKiernan, M. J.; Halls, J. J. M.; Greenham, N. C.; Friend, R. H. Dual Electron Donor/Electron Acceptor Character of a Conjugated Polymer in Efficient Photovoltaic Diodes. *Appl. Phys. Lett.* **2007**, *90*, 193506.
5. Markov, D. E.; Amsterdam, E.; Blom, P. W. M.; Sieval, A. B.; Hummelen, J. C. Accurate Measurement of the Exciton Diffusion Length in a Conjugated Polymer Using a Heterostructure with a Side-Chain Cross-Linked Fullerene Layer. *J. Phys. Chem. A* **2005**, *109*, 5266–5274.
6. Yang, X.; Loos, J. Toward High-Performance Polymer Solar Cells: The Importance of Morphology Control. *Macromolecules* **2007**, *40*, 1353–1362.
7. Moulé, A. J.; Meerholz, K. Morphology Control in Solution-Processed Bulk-Heterojunction Solar Cell Mixtures. *Adv. Funct. Mater.* **2009**, *19*, 3028–3036.
8. Veenstra, S. C.; Loos, J.; Kroon, J. M. Nanoscale Structure of Solar Cells Based on Pure Conjugated Polymer Blends. *Prog. Photovoltaics* **2007**, *15*, 727–740.
9. McNeill, C. R.; Westenhoff, S.; Groves, C.; Friend, R. H.; Greenham, N. C. Influence of Nanoscale Phase Separation on the Charge Generation Dynamics and Photovoltaic Performance of Conjugated Polymer Blends—Balancing Charge Generation and Separation. *J. Phys. Chem. C* **2007**, *111*, 19153–19160.

10. Westenhoff, S.; Howard, I. A.; Friend, R. H. Probing the Morphology and Energy Landscape of Blends of Conjugated Polymers with Sub-10 nm Resolution. *Phys. Rev. Lett.* **2008**, *101*, 016102.
11. Groves, C.; Marsh, R. A.; Greenham, N. C. Monte Carlo Modeling of Geminate Recombination in Polymer−Polymer Photovoltaic Devices. *J. Chem. Phys.* **2008**, *129*, 114903.
12. Veldman, D.; Ipek, O.; Meskers, S. C. J.; Sweelssen, J.; Koetse, M. M.; Veenstra, S. C.; Kroon, J. M.; van Bavel, S. S.; Loos, J.; Janssen, R. A. J. Compositional and Electric Field Dependence of the Dissociation of Charge Transfer Excitons in Alternating Polyfluorene Copolymer/Fullerene Blends. *J. Am. Chem. Soc.* **2008**, *130*, 7721–7735.
13. Watkins, P. K.; Walker, A. B.; Verschoor, G. L. B. Dynamical Monte Carlo Modelling of Organic Solar Cells: The Dependance of Internal Quantum Efficiency on Morphology. *Nano Lett.* **2005**, *5*, 1814–1818.
14. He, Z.; Zhong, C.; Huang, X.; Wong., W.-Y.; Wu, H.; Chen, L.; Su, S.; Cao, Y. Simultaneous Enhancement of Open-Circuit Voltage, Short-Circuit Current Density, and Fill Factor in Polymer Solar Cells. *Adv. Mater.* **2011**, *23*, 4636–4643.
15. Granström, M.; Petritsch, K.; Arias, A. C.; Lux, A.; Andersson, M. R.; Friend, R. H. Laminated Fabrication of Polymeric Photovoltaic Diodes. *Nature* **1998**, *395*, 257.
16. Holcombe, T. W.; Woo, C. H.; Kavulak, D. F. J.; Thompson, B. C.; Frechet, J. M. J. All-Polymer Photovoltaic Devices of Poly(3-(4-*N*-octyl)-phenylthiophene) from Grignard Metathesis (Grim) Polymerization. *J. Am. Chem. Soc.* **2009**, *131*, 14160–14161.
17. Kietzke, T.; Hörhold, H.-H.; Neher, D. Efficient Polymer Solar Cells Based on M3EH-PPV. *Chem. Mater.* **2005**, *17*, 6532–6537.
18. Koetse, M. M.; Sweelssen, J.; Hoekerd, K. T.; Schoo, H. F. M.; Veenstra, S. C.; Kroon, J. M.; Yang, X.; Loos, J. Efficient Polymer:Polymer Bulk Heterojunction Solar Cells. *Appl. Phys. Lett.* **2006**, *88*, 083504.
19. Hodgkiss, J. M.; Campbell, A. R.; Marsh, R. A.; Rao, A.; Albert-Seifried, S.; Friend, R. H. Subnanosecond Geminate Charge Recombination in Polymer−Polymer Photovoltaic Devices. *Phys. Rev. Lett.* **2010**, *104*, 177701.
20. Mandoc, M. M.; Veurman, W.; Koster, L. J. A.; de Boer, B.; Blom, P. W. M. Origin of the Reduced Fill Factor and Photocurrent in MDMO-PPV:PCNEPV All-Polymer Solar Cells. *Adv. Funct. Mater.* **2007**, *17*, 2167–2173.
21. Moore, J. R.; Albert-Seifried, S.; Rao, A.; Massip, S.; Watts, B.; Morgan, D. J.; Friend, R. H.; McNeill, C. R.; Sirringhaus, H. Polymer Blend Solar Cells Based on a High-Mobility Naphthalenediimide-Based Polymer Acceptor: Device Physics, Photophysics and Morphology. *Adv. Energy Mater.* **2011**, *1*, 230–240.
22. Yin, C.; Kietzke, T.; Neher, D.; Hörhold, H. H. Photovoltaic Properties and Exciplex Emission of Polyphenylenevinylene-Based Blend Solar Cells. *Appl. Phys. Lett.* **2007**, *90*, 092117.
23. Collins, B. A.; Gann, E.; Guignard, L.; He, X.; McNeill, C. R.; Ade, H. Molecular Miscibility of Polymer-Fullerene Blends. *J. Phys. Chem . Lett.* **2010**, *1*, 3160–3166.
24. Parnell, A. J.; Cadby, A. J.; Mykhaylyk, O. O.; Dunbar, A. D. F.; Hopkinson, P. E.; Donald, A. M.; Jones, R. A. L. Nanoscale Phase Separation of P3HT PCBM Thick Films as Measured by Small-Angle X-ray Scattering. *Macromolecules* **2011**, *44*, 6503–6508.
25. Treat, N. D.; Brady, M. A.; Smith, G.; Toney, M. F.; Kramer, E. J.; Hawker, C. J.; Chabinyc, M. L. Interdiffusion of PCBM and P3HT Reveals Miscibility in a Photovoltaically Active Blend. *Adv. Energy Mater.* **2011**, *1*, 82–89.
26. Yin, W.; Dadmun, M. A New Model for the Morphology of P3HT/PCBM Organic Photovoltaics from Small-Angle Neutron Scattering: Rivers and Streams. *ACS Nano* **2011**, *5*, 4756–4768.
27. Martens, T.; D'Haen, J.; Munters, T.; Beelen, Z.; Goris, L.; Manca, J.; D'Olieslaeger, M.; Vanderzande, D.; de Schepper, L.; Andriessen, R. Disclosure of the Nanostructure of MDMO-PPV:PCBM Bulk Hetero-Junction Organic Solar Cells by a Combination of SPM and TEM. *Synth. Met.* **2003**, *138*, 243–247.
28. van Bavel, S. S.; Sourty, S.; de With, G.; Loos, J. Three-Dimensional Nanoscale Organization of Bulk Heterojunction Polymer Solar Cells. *Nano Lett.* **2009**, *9*, 507–513.
29. Yang, X.; Loos, J.; Veenstra, S. C.; Verhees, W. J. H.; Wienk, M. M.; Kroon, J. M.; Michels, M. A. J.; Janssen, R. A. J. Nanoscale Morphology of High-Performance Polymer Solar Cells. *Nano Lett.* **2005**, *5*, 579–583.
30. Li, G.; Shrotriya, V.; Huang, J.; Yao, Y.; Moriarty, T.; Emery, K.; Yang, Y. High-Efficiency Solution Processable Polymer Photovoltaic Cells by Self-Organization of Polymer Blends. *Nat. Mater.* **2005**, *4*, 864–868.
31. Shaheen, S. E.; Brabec, C. J.; Sariciftci, N. S.; Padinger, F.; Fromherz, T.; Hummelen, J. C. 2.5% Efficient Organic Plastic Solar Cells. *Appl. Phys. Lett.* **2001**, *78*, 841–843.
32. Drummy, L. F.; Davis, R. J.; Moore, D. L.; Durstock, M.; Vaia, R. A.; Hsu, J. W. P. Molecular-Scale and Nanoscale Morphology of P3HT:PCBM Bulk Heterojunctions: Energy-Filtered TEM and Low-Dose HREM. *Chem. Mater.* **2011**, *23*, 907–912.
33. Herzing, A. A.; Richter, L. J.; Anderson, I. M. 3D Nanoscale Characterization of Thin-Film Organic Photovoltaic Device Structures *via* Spectroscopic Contrast in the TEM. *J. Phys. Chem. C* **2011**, *114*, 17501–17508.
34. Veenstra, S. C.; Verhees, W. J. H.; Kroon, J. M.; Koetse, M. M.; Sweelssen, J.; Bastiaansen, J. J. A. M.; Schoo, H. F. M.; Yang, X.; Alexeev, A.; Loos, J.; *et al.* Photovoltaic Properties of a Conjugated Polymer Blend of MDMO-PPV and PCNEPV. *Chem. Mater.* **2004**, *16*, 2503–2508.
35. Kozub, D. R.; Vakhshouri, K.; Orme, L. M.; Wang, C.; Hexemer, A.; Gomez, E. D. Polymer Crystallization of Partially Miscible Polythiophene/Fullerene Mixtures Controls Morphology. *Macromolecules* **2011**, *44*, 5722–5726.
36. Kiel, J. W.; Eberle, A. P. R; Mackay, M. E. Nanoparticle Agglomeration in Polymer-Based Solar Cells. *Phys. Rev. Lett.* **2010**, *105*, 168701.
37. Chen, D.; Liu, F.; Wang, C.; Nakahara, A.; Russell, T. P. Bulk Heterojunction Photovoltaic Active Layers *via* Bilayer Interdiffusion. *Nano Lett.* **2011**, *11*, 2071–2078.
38. Agostinelli, T.; Lilliu, S.; Labram, J. G.; Campoy-Quiles, M.; Hampton, M.; Pires, E.; Rawle, J.; Bikondoa, O.; Bradley, D. D. C.; Anthopoulos, T. D.; *et al.* Real-Time Investigation of Crystallization and Phase-Segregation Dynamics in P3HT: PCBM Solar Cells during Thermal Annealing. *Adv. Funct. Mater.* **2011**, *21*, 1701–1708.
39. Gomez, E. D.; Barteau, K. P.; Wang, H.; Toney, M. F.; Loo, Y.-L. Correlating the Scattered Intensities of P3HT and PCBM to the Current Densities of Polymer Solar Cells. *Chem. Commun.* **2011**, *47*, 436–438.
40. Ade, H.; Hitchcock, A. NEXAFS Microscopy and Resonant Scattering: Composition and Orientation Probed in Real and Reciprocal Space. *Polymer* **2008**, *49*, 643–675.
41. Swaraj, S.; Wang, C.; Araki, T.; Mitchell, G. E.; Liu, L.; Gaynor, S.; Deshmukh, B.; Yan, Y.; McNeill, C. R.; Ade, H. The Utility of Resonant Soft X-ray Scattering and Reflectivity for the Nanoscale Characterization of Polymers. *Eur. Phys. J. Special Topics* **2009**, *168*, 121–126.
42. Ade, H.; Zhang, X.; Cameron, S.; Costello, C.; Kirz, J.; Williams, S. Chemical Contrast in X-ray Microscopy and Spatially Resolved XANES Spectroscopy of Organic Specimens. *Science* **1992**, *258*, 972–975.
43. McNeill, C. R.; Watts, B.; Swaraj, S.; Ade, H.; Thomsen, L.; Belcher, W. J.; Dastoor, P. C. Evolution of the Nanomorphology of Photovoltaic Polyfluorene Blends: Sub-100 nm Resolution with X-ray Spectromicroscopy. *Nanotechnology* **2008**, *19*, 424015.
44. McNeill, C. R.; Watts, B.; Thomsen, L.; Belcher, W. J.; Kilcoyne, A. K. D.; Greenham, N. C.; Dastoor, P. C. X-ray Spectromicroscopy of Polymer/Fullerene Composites: Quantitative Chemical Mapping. *Small* **2006**, *2*, 1432–1435.
45. Swaraj, S.; Wang, C.; Yan, H.; Watts, B.; Lüning, J.; McNeill, C. R.; Ade, H. Nanomorphology of Bulk Heterojunction Photovoltaic Thin Films Probed with Resonant Soft X-ray Scattering. *Nano Lett.* **2010**, *10*, 2863–2869.
46. Yan, H.; Chen, Z.; Zheng, Y.; Newman, C.; Quinn, J. R.; Dötz, F.; Kastler, M.; Facchetti, A. A High-Mobility Electron-Transporting Polymer for Printed Transistors. *Nature* **2009**, *457*, 679–687.

47. Clark, J.; Silva, C.; Friend, R. H.; Spano, F. Role of Intermolecular Coupling in the Photophysics of Disordered Organic Semiconductors: Aggregate Emission in Regioregular Polythiophene. *Phys. Rev. Lett.* **2007**, *98*, 206406.
48. Schuettfort, T.; Huettner, S.; Lilliu, S.; Macdonald, J. E.; Thomsen, L.; McNeill, C. R. Surface and Bulk Structural Characterization of a High-Mobility Electron-Transporting Polymer. *Macromolecules* **2011**, *44*, 1530–1539.
49. Flesch, H.-G.; Resel, R.; McNeill, C. R. Charge Transport Properties and Microstructure of Polythiophene/Polyfluorene Blends. *Org. Electron.* **2009**, *10*, 1549–1555.
50. McNeill, C. R.; Abrusci, A.; Hwang, I.; Ruderer, M.; Müller-Buschbaum, P.; Greenham, N. C. Photophysics and Photocurrent Generation in Polythiophene/Polyfluorene Copolymer Blends. *Adv. Funct. Mater.* **2009**, *19*, 3103–3111.
51. Verploegen, E.; Mondal, R.; Bettinger, C. J.; Sok, S.; Toney, M. F.; Bao, Z. Effects of Thermal Annealing upon the Morphology of Polymer–Fullerene Blends. *Adv. Funct. Mater.* **2010**, *20*, 3519–3529.
52. McNeill, C. R.; Halls, J. J. M.; Wilson, R.; Whiting, G. L.; Berkebile, S.; Ramsey, M. G.; Friend, R. H.; Greenham, N. C. Efficient Polythiophene/Polyfluorene Co-polymer Bulk Heterojunction Photovoltaic Devices: Device Physics and Annealing Effects. *Adv. Funct. Mater.* **2008**, *18*, 2309–2321.
53. Chen, W.; Xu, T.; He, F.; Wang, W.; Wang, C.; Strzalka, J.; Liu, Y.; Wen, J.; Miller, D. J.; Chen, J.; *et al.* Hierarchical Nanomorphologies Promote Exciton Dissociation in Polymer/Fullerene Bulk Heterojunction Solar Cells. *Nano Lett.* **2011**, *11*, 3707–3713.
54. Wagenpfahl, A.; Rauh, D.; Binder, M.; Deibel, C.; Dyakonov, V. S-Shaped Current-Voltage Characteristics of Organic Solar Devices. *Phys. Rev. B* **2010**, *82*, 115306.
55. Fabiano, S.; Chen, Z.; Vahedi, S.; Facchetti, A.; Pignataro, B.; Loi, M. A. Role of Photoactive Layer Morphology in High Fill Factor All-Polymer Bulk Heterojunction Solar Cells. *J. Mater. Chem.* **2011**, *21*, 5891–5896.
56. Wang, C.; Hexemer, A.; Nasiatka, J.; Chan, E. R.; Young, A. T.; Padmore, H. A.; Schlotter, W. F.; Lüning, J.; Swaraj, S.; Watts, B.; *et al.* Resonant Soft X-ray Scattering of Polymers with a 2D Detector: Initial Results and System Developments at the Advanced Light Source. *IOP Conf. Ser.: Mater. Sci. Eng.* **2010**, *14*, 012016.
57. Hexemer, A.; Bras, W.; Glossinger, J.; Schaible, E.; Gann, E.; Kirian, R.; MacDowell, A.; Church, M.; Rude, B.; Padmore, H. A SAXS/WAXS/GISAXS Beamline with Multilayer Monochromator. *J. Phys.: Conf. Ser.* **2010**, *247*, 012007.
58. Kilcoyne, A. L. D.; Tyliszczak, T.; Steele, W. F.; Fakra, S.; Hitchcock, P.; Franck, K.; Anderson, E. H.; Harteneck, B. D.; Rightor, E. G.; Mitchell, G. E.; *et al.* Interferometer Controlled Scanning Transmission X-ray Microscopes at the Advanced Light Source. *J. Synchrotron Radiat.* **2003**, *10*, 125–136.